



# The TES beamline (8-BM) at NSLS-II: tender-energy spatially resolved X-ray absorption spectroscopy and X-ray fluorescence imaging

**Paul Northrup**

*J. Synchrotron Rad.* (2019). **26**, 2064–2074



**IUCr Journals**

CRYSTALLOGRAPHY JOURNALS ONLINE

Copyright © International Union of Crystallography

Author(s) of this article may load this reprint on their own web site or institutional repository provided that this cover page is retained. Republication of this article or its storage in electronic databases other than as specified above is not permitted without prior permission in writing from the IUCr.

For further information see <http://journals.iucr.org/services/authorrights.html>

# The TES beamline (8-BM) at NSLS-II: tender-energy spatially resolved X-ray absorption spectroscopy and X-ray fluorescence imaging

Paul Northrup\*

National Synchrotron Light Source II, Brookhaven National Laboratory, Upton, NY 11973, USA, and  
Department of Geosciences, Stony Brook University, Stony Brook, NY 11794, USA.

\*Correspondence e-mail: paul.northrup@stonybrook.edu

Received 15 May 2019

Accepted 13 September 2019

Edited by I. Lindau, SLAC/Stanford University, USA

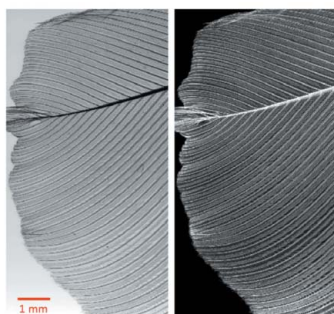
**Keywords:** tender energy; microbeam XAS; *in situ* XAS; XRF microprobes; XANES; EXAFS; NSLS-II.

**Supporting information:** this article has supporting information at journals.iucr.org/s

The tender-energy X-ray spectroscopy (TES) beamline at the National Synchrotron Light Source II (NSLS-II) is now operational for general users. Its scientific mission includes static and *in situ* X-ray fluorescence imaging and spatially resolved X-ray absorption spectroscopy for characterization of complex heterogeneous, structured and dynamic natural or engineered materials and systems. TES is optimized for the tender-energy range, offering routine operations from 2.0 to 5.5 keV, with capabilities to reach down to 1.2 or up to 8 keV with configuration change. TES is designed as an extended X-ray absorption fine-structure microprobe (EXAFS microprobe) for applications of micrometre-scale EXAFS spectroscopy to heterogeneous samples. Beam size is user-tunable from  $\sim 2$  to 25  $\mu\text{m}$ . Energy may be scanned on-the-fly or in traditional step scanning. Importantly, the position of the microbeam at the sample location does not move significantly during energy scanning or when changing energy across the entire routine energy range. This enables full EXAFS of a particle or domain the same size as the probe beam, and measurement of the same spot at different energies. In addition, there is no measurable drift in energy calibration (repeatability) scan-to-scan and over 24 h. This is critical where simultaneous calibration measurements are generally not feasible, and for speciation mapping where precise and stable control of incident energy is essential. The sample environment is helium atmosphere at room pressure with infrastructure for *in situ* electrochemistry and catalysis in small sample cells or microreactors. As the first bend-magnet beamline at NSLS-II, noteworthy commissioning aspects are described. Example measurements are presented to illustrate its capabilities.

## 1. Introduction

Hard X-ray fluorescence (XRF) microprobes provide capabilities for element-specific qualitative (and sometimes quantitative) mapping of the distributions and associations of different elements. Measurements are generally non-destructive and require minimal sample preparation. Element-specific chemistry can be probed using accessory X-ray absorption spectroscopy (XAS); X-ray absorption near-edge structure (XANES) can identify the oxidation state and speciation. Speciation imaging can be used in some cases to map the distribution of different chemical species by setting the incident energy to that of a specific XANES feature. In comparison, bulk XAS beamlines offer XANES and extended X-ray absorption fine structure (EXAFS). Fluorescence EXAFS measurements are more demanding but provide details about local structure (coordination and short-range interatomic distances) in crystalline or non-crystalline materials.



Most fluorescence microprobe and XAS beamlines are optimized in the hard X-ray regime ( $>5$  keV), and may extend into the tender range with less than optimal performance, but scientific interest in lighter elements not reachable with hard X-rays has been growing. Accessible absorption edges in the tender-energy X-ray spectroscopy (TES) energy range are (1) *K*-edges of Mg, Al, Si, P, S, Cl, K, Ca and Ti, which are important elements in soil and environmental sciences (e.g. plant-root-microbe systems), geologic and cosmologic materials, energy-related functional materials and devices (e.g. energy storage, photovoltaics, fuel cells and catalysts), biological systems, and systems critical to or impacted by climate change (including terrestrial, atmospheric and marine components); (2) *L*-edges of As through I, including important metals for novel materials and superconductors, mineral resources, environmental contaminants and biological toxins; and (3) *M*-edges of heavy REEs through Pu, including radionuclides of environmental concern, Pt and other catalysts, and metals important to functional nanomaterials. Some applications are summarized by Akabayov *et al.* (2005) and Northrup *et al.* (2016). A few examples illustrating diverse applications include P in sediments (Diaz *et al.*, 2008); Ca in alfalfa (Punshon *et al.*, 2013); Sb in semiconductors (Voyles *et al.*, 2003) and plastic water bottles (Martin *et al.*, 2010); S in petroleum (George & Gorbaty, 1989), coal (Bolin *et al.*, 2016), fuel cells (Baturina *et al.*, 2013) and amber (Riquelme *et al.*, 2014); and Zr and S in catalysts (Liu *et al.*, 2014).

Efforts to expand existing hard X-ray programs of *in situ* and *operando* XAS in catalysis and electrochemistry toward progressively lower energy face increasing challenges because of window materials, path lengths through air or gas, and sample geometries. Based on these challenges, and in collaboration with the catalysis user community, the TES program employs small or microscale reaction cells (e.g. Li *et al.*, 2015) utilizing small sample volumes and a small beam footprint. Since such samples are more likely to be heterogeneous on the scale of the beam, EXAFS measurements of these require strict beam-positional stability during scanning.

The scientific drivers for TES grew out of the lower-energy programs at NSLS X15B and X19A (bulk XAS), and the X26A and X27A hard X-ray microprobes. However, the transition to NSLS-II offered opportunities to not only upgrade optics and improve the performance of existing NSLS capabilities but also to create new capabilities that take advantage of the NSLS-II source properties. In particular, the vision for TES was to bring full XAFS capabilities down to the microscale without compromising energy scanning to achieve microfocus. Toward that end, a Kirkpatrick–Baez (KB) based microbeam endstation for TES was designed, constructed and commissioned at X15B during the last year of operation of NSLS. The TES user community was assembled and cultivated through the efforts of beamline scientists and a number of workshops (e.g. Lanzirotti *et al.*, 2007; Northrup *et al.*, 2007). These efforts culminated in a successful beamline development proposal (Northrup *et al.*, 2010).

The effort to build out non-ID beamlines, transition NSLS programs to NSLS-II and provide early user capacity at

NSLS-II was originally organized as the NxtGen portfolio under E. Johnson but was delayed by the priority of ID beamlines and limitations to financial and technical resources. In 2013, NxtGen was reorganized into the BDN (Beamlines Developed by NSLS-II) project under J. Adams and ultimately delivered five beamlines on bend magnet (BM) ports, utilizing three-pole-wiggler or BM sources. As such, TES utilized as much hardware from NSLS as possible (Ivashkevych *et al.*, 2018), with appropriate upgrades, refurbishment and all new optical surfaces. TES also benefited from investment by several partner users beginning in 2010. The Tender Energy Microspectroscopy Consortium incorporated funding from instrumentation grants (NSF, Northrup *et al.*, 2013; DOE, Northrup, 2013; NASA, Northrup & Flynn 2012), assets from Bell Laboratories and design effort funded by member institutions. These resources enabled the purchase of long-lead-time components and construction of the TES endstation before funding was available to start the BDN project.

## 2. Optical design

XAS and XRF in the tender-energy range require specific optimizations of beamline design that are different from the approaches taken by facilities optimized for either hard or soft X-rays as follows. Firstly, the source must have a low critical energy. Also, optics operate at higher incidence angles requiring geometric consideration, and specialized monochromator crystals and high-angular-range monochromator design are needed. Harmonic rejection also requires particular attention and mirror coatings must avoid absorption edges such as Rh *L* and Pt *M*. Windows and beam-position monitors (BPMs) must also be transparent to lower energy. When samples are not vacuum compatible, the sample environment must be helium. Finally, sample mountings and *in situ* cells must be designed for low-energy transparency and consequent small sample sizes.

XRF imaging requires good optical performance for high flux density in small spot sizes. However, since XAS requires a broadband source and low coherence, this precludes use of an undulator source at NSLS-II. It also necessitates achromatic optics. The objective of TES, microscale characterization, is best served by a versatile spot size in the  $\sim 2$  to 25  $\mu\text{m}$  range.

Spatially resolved EXAFS likewise requires optimization of beamline design that is distinct from either bulk-XAS beamlines or typical imaging beamlines (even those with some spectroscopy capabilities). The unique capabilities and requirements that define an EXAFS microprobe, such as TES and its hard X-ray sister beamline XFM, include the following. A versatile spot size is necessary to match beam footprint to the area to be measured; the beamline must deliver quality fluorescence EXAFS at all available spot sizes. The ultimate challenge is full EXAFS of a particle or domain the same size as the probe microbeam. To achieve this, the beam on the sample must not significantly change position, size, shape, flux distribution, energy distribution or harmonics distribution, over an energy scan of up to 1000 eV or when changing energy between different absorption edges such as P and Ca. This

**Table 1**  
TES specifications.

Energy range	Optimized for 2.0–5.5 keV, down to ~1 keV or up to ~8 keV with configuration change
Spot size	User-tunable microbeam from 2 to 25 $\mu\text{m}$ , or millimetre-size unfocused
Flux	Up to $10^{11}$ photons $\text{s}^{-1}$ at 500 mA, depending on beam size and energy
Energy scanning	Up to 1000 eV, in both step and on-the-fly modes
Positional stability	Within ~5% of spot size, independent of energy, over 12+ hours
Energy stability/repeatability	No measureable drift or variation of calibration, scan-to-scan and over 24+ hours
Sample environment	Helium atmosphere, accommodations for <i>in situ</i> cells

places very high demands on stability of both the beamline optics and the beam source. It is also important that the microbeam be cleanly defined without significant tails, so as to make measurements of low-concentration areas near high-concentration spots. A long working distance is needed to accommodate *in situ* measurements and large or odd-shaped samples. Combined XAFS/XRF imaging can include both image-stack and energy-scan-per-pixel modes, or mapping at species-selective energies to perform oxidation-state mapping or speciation imaging. Fast on-the-fly energy scanning is critical for measurements of species or samples subject to beam damage or alteration. Often the best way to study damage-susceptible species is to use spectroscopic imaging to minimize the dose to any given pixel. A prerequisite for spectroscopic imaging is that energy calibration be stable and repeatable.

In order to meet the needs of its driving science programs, as well as the technical requirements for tender-energy and spatially resolved XAS described above, TES is designed to deliver the specifications given in Table 1. Originally presented as an ideal use of the soft-bend sources of the proposed NSLS-II facility in 2007, TES conceptual design was developed within the BNL/Stony Brook Center for Environmental Molecular Science. Further design and testing included input from S. Hulbert and collaboration with R. Tappero (X27A and XFM beamlines). Beamline layout at NSLS-II was finalized and documented with assistance from E. Haas, L. Lienhard, M. Carlucci-Dayton, M. Johanson, W. Wilds and S. Restmeyer. The overall optical layout is described in Table 2. All mirrors are Ni-coated Si so as to not have any absorption edges in the energy range from 1 to 8 keV. The entire beamline up to the endstation is ultrahigh vacuum and windowless.

The overall optical design uses compound focusing to gather a large fan of radiation into a versatile microfocus, while incorporating the essentials for EXAFS energy scanning including collimation and harmonic rejection, and utilizing a fixed-exit and feedback-stabilized monochromator to maintain alignment and stable performance when scanning or changing energy. TES design began with the classic EXAFS beamline layout of vertically collimating mirror, monochromator, focusing mirror and sample. The collimating mirror is far enough upstream to accept the full vertical fan

**Table 2**  
TES optical components layout.

		Distance (m) from source
Source point, 3.25 mrad into bend	Inside accelerator tunnel	—
White beam slits		10
Mirror 1, vertically collimating		11.0
Mirror 2, redirecting		12.3
Monochromator, fixed-exit double crystal	In first optical enclosure	25
Mirror 3, focusing toroid		26.57
SSA	On experimental floor	53.14
KB mirror system	Inside helium-atmosphere endstation	56.8
Sample position		57.14

from the BM source. A redirecting mirror maintains the horizontal beam and allows for fixed-exit use of the two mirrors at different pitch settings depending on harmonic rejection needs. The monochromator then receives a vertically collimated beam for optimal energy resolution and a large beam footprint with low power density; it is as far upstream as possible to maximize horizontal acceptance of the focusing mirror. These components are optimized for energy scanning; remaining optical components convey these XAS capabilities down to the microscale. A toroidal mirror focuses the beam to the Secondary Source Aperture (SSA), which provides a virtual source for microfocusing optics and allows users to easily tune spot size. Final focusing to the sample position is provided by horizontal and vertical focusing mirrors (HFM and VFM) in the KB geometry. An important design consideration was whether to use bender-style or fixed-curvature mirrors. Since the upstream collimating and macro-focusing mirrors have tunable bends, the precise divergence distribution of beam coming to the KB mirrors will vary. Therefore, the curvature of the KB mirrors must be asymmetrically tunable in order to achieve optimal focus and this can only be accomplished with bender-style mirrors.

The primary focusing mirror is chosen to be a 1:1 toroid, pushing the beamline to the end of the available floor length, in part to minimize divergence and maximize acceptance of the KB mirrors. Another reason to use a 1:1 toroid for primary focusing is to reduce optical aberration at the sample position. As pointed out by MacDowell *et al.* (2004), when using a toroid after a vertically collimating mirror, a 1:1 toroid will produce significant optical aberration at its focus. They demonstrated that a 2:1 geometry is preferred, as it effectively cancels out such aberrations at the focal point and produces a much better focus. While that would be preferred if beam were to be utilized at that location, the TES design produces less aberration at the microfocus by effectively using the SSA to filter out the aberration from the 1:1 toroid before passing the beam to the microfocusing optics (Fig. 1). As a result, the

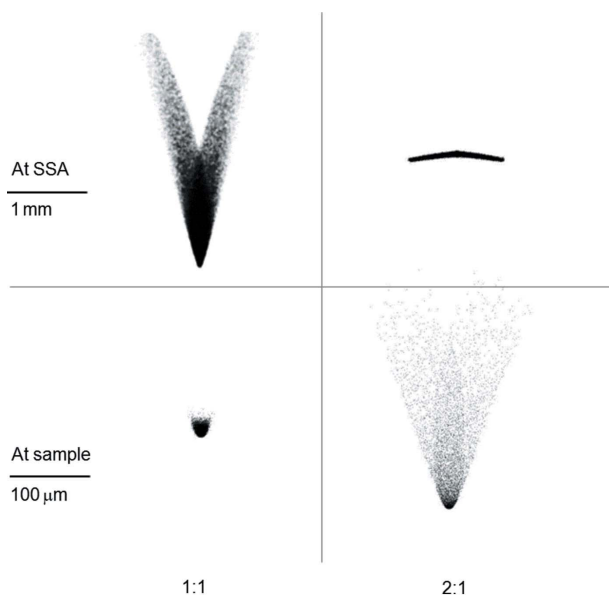


**Figure 1** Raytracing models (*Shadow* software; Sanchez del Rio *et al.*, 2011) for 1:1 (TES) versus 2:1 toroidal focusing. Beam footprint at primary focus, showing substantial aberration for 1:1 and superiority of the 2:1 focus at that location (top). Corresponding microbeam focus at sample position with SSA adjusted to pass 50% of photons (bottom).

microfocused beam at TES using the 1:1 toroid is very clean and crisply defined, particularly at smaller spot sizes.

Another important reason for the 1:1 beamline length is to decouple instability, mechanical variation with energy, or vibration of the optics (or source) from the beam position at the sample location. Because the primary optics are so far from the SSA, beam position at the sample will be dictated primarily by the static stability of the SSA and endstation, both of which are mounted on granite and located in close proximity. Any instability upstream will translate into fluctuations of intensity, *i.e.* throughput of the SSA, rather than fluctuations of beam position.

While this provides the required positional stability of the microbeam at the sample, it does create a different but acute sensitivity to instability, in that the beam may move off the SSA and cause intensity fluctuations or loss of beam to the sample. The 28 m lever arm from the monochromator to the SSA amplifies these effects as it only takes a few microradians of variation to move the beam 0.1 mm at the SSA (its typical opening size). This, coupled with the large angular travel of the monochromator, therefore necessitates the use of positional feedbacks to maintain beam position at different energies and during energy scanning. Separate vertical and horizontal BPMs near the point of focus are used for feedback. Vertical feedback actuates fine pitch adjustment of the first monochromator crystal; horizontal feedback actuates fine roll adjustment of the second crystal.

A related design consideration is energy-calibration stability (repeatability). By defining the beam vertical position exiting the monochromator and locking its location at the SSA, this sets the angle of beam relative to the second crystal of the monochromator. The monochromator mechanism

directly drives the second crystal, and the second crystal has no pitch adjustment or thermal load; the angle of the beam from the second crystal to the SSA defines energy calibration. Typical sources of instability, such as thermal changes to the first crystal, are compensated by feedback-driven adjustment of first-crystal fine pitch, maintaining that angle. As pointed out by L. Berman (personal communication), this approach may still induce a change in energy calibration; but even in the worst case, the full range of travel of the fine pitch adjustment would change energy calibration less than 0.01 eV. Within our ability to determine, there is no measurable drift or variation of energy calibration at TES, with positional feedback operational, scan-to-scan and over >24 h. This permits users to run their entire experiments with only a few energy-calibration measurements.

The net result of TES design is high flux density in a well behaved and tunable microbeam with full energy-scanning capabilities. The following paragraphs detail individual components and subsystems.

(1) Source and front-end. TES is the only NSLS-II beamline to date that uses only a dipole bend magnet as its X-ray source. This choice is based on the ideal characteristics of an NSLS-II BM: a critical energy of 2.39 keV which reduces unwanted high-energy power, a broadband photon spectrum needed for energy scanning, a small source ideal for focusing applications, a low coherence for XAS, and nearly uniform photon and heatload distributions across the large usable beam footprint. Its primary drawback is that the accessible source is at only 3.25 mrad into the bend, before the field reaches full intensity. However, this has only a minor impact, as the resulting asymmetry in flux distribution is limited below 5 keV and asymmetry in power distribution is within  $\sim 10\%$ . The generic design of front-end components for BM and 3PW beamlines (Hussain, 2014) consists of masks to define the synchrotron radiation fan, Bremsstrahlung collimators and white-beam slits. Specific design of the TES front-end (in collaboration with A. Hussain, S. Sharma, G. Dacos and F. De Paolo) included Mirrors 1 and 2, an additional collimator for the offset beam, and diagnostics for mirror alignment. Radiation-shielding requirements played an important role in beamline and optical design, in order to safely separate the useful photon beam from coincident higher-energy synchrotron, Bremsstrahlung and electron-loss radiation.

(2) Mirror 1 and Mirror 2. Mirror 1 is used for vertical collimation; Mirrors 1 and 2 serve as low-pass filters for harmonic rejection and to protect sensitive monochromator crystals by operating at a range of pitch to provide an appropriate energy cut-off. Optical and physical specifications are given in Table 3. Mirror 1 is an optical flat with tunable bend and deflects the beam downward. The primary purpose of Mirror 2, an upward-deflecting optical flat, is to redirect the beam so as to exit parallel to the BM beam centerline but 25 mm lower. The length of Mirror 2 permits maintenance of the constant beam offset over the full range of pitch by shifting the beam along the lengths of Mirrors 1 and 2. Although nominally flat, Mirror 2 has some curvature because of gravity sag and so partly contributes to beam collimation; the bend

**Table 3**  
Specifications of TES large mirrors.

	Mirror 1	Mirror 2	Mirror 3
Type	Flat with bender	Flat	Cylinder with bender, sagittal radius 186 mm
Size	813 mm long, 100 mm wide, 60 mm thick	1.2 m long, 70 mm wide, 40 mm thick	960 mm long, 100 mm wide, 80 mm thick
Optical quality	0.40 $\mu$ rad slope error, 0.2 nm roughness	0.36 $\mu$ rad slope error, 0.18 nm roughness	1.06 $\mu$ rad slope error, 0.5 nm roughness
Pitch	6.8 to 20 mrad	6.8 to 20 mrad	7 mrad
Operational heatload	4 to 24 W	3 to 6 W	—

of Mirror 1 is adjusted to provide the appropriate net collimation.

The chamber and mechanism for Mirror 1 was previously in service at NSLS X15B. The former Glidcop mirror was replaced with a new silicon substrate. Detailed analysis of the mounting and bender stresses on the Si mirror demonstrated that its greater stiffness is offset by the longer distance to the source requiring less bending, and both the bend stress and contact pressure are well within the safe range for Si. Finite-element analysis confirmed that thermal distortions are not significant and are fully compensated by optics. The power load is constant during normal top-off operation.

Mirror 2 is a new system, designed in collaboration with S. Cheeseman and N. Andrade at Kurt Lesker Co., and T. Tonnessen at InSync. A new cooling system was designed and implemented for both mirrors that uses braid cooling attached to copper rods connected to heat exchangers outside of vacuum. Polished copper interface blocks attach to the back of the mirror substrates using bolts to nut rods in transverse holes drilled through the mirrors. This eliminates any in-vacuum water connections and isolates the mirror from vibrations of the water system.

(3) Monochromator. The TES monochromator is a fixed-exit double-crystal design from NSLS X15B, refurbished and tested to deliver the required capabilities. Theta can be scanned from 10 to 80° by moving a single external linear drive; this motion translates the second crystal parallel to the exit beam and is converted into coordinated rotation of each crystal (MacDowell *et al.*, 1988, 1989; Rowen *et al.*, 1986). The beam footprint is up to 5 mm vertical  $\times$  65 mm horizontal. Coarse adjustments of first-crystal pitch and roll are in-vacuum motors. Fine adjustment to first-crystal pitch employs a solenoid mechanism that ties into the optics feedback system. Commissioning confirmed the need for an additional fine roll adjustment, which was implemented for the second crystal. This new design uses a compound lever geometry with picomotor actuation for control of horizontal beam trajectory within 100 nrad (see the supporting information for details).

The first crystal is indirectly water cooled. Just upstream of the monochromator is a 2.9  $\mu$ m graphite filter which absorbs low-energy power. The standard configuration uses Si(111) crystals for 2.0 keV and upwards. Other sets for energy <2 keV, not yet commissioned at this writing, include InSb(111), quartz and beryl. Crystals are easily exchanged, with access to the vacuum vessel. Beryl crystals are considered susceptible to radiation damage but tests at X15B showed that no measurable degradation occurred after >2 months exposure provided the incident beam was limited to <4 keV.

Because the source size at NSLS-II is so small, crystal surface quality is particularly important to optical performance; crystal distortion must also be minimized. The monochromator is not intentionally detuned for harmonic rejection because the first mirrors provide a tunable energy cut-off.

Energy scanning is conducted in either step or on-the-fly modes. Both move unidirectionally from low to high energy; the monochromator is designed to deliver its greatest mechanical stability in that direction. For step scanning, sufficient settling time is included to dampen any vibration of the first-crystal pitch. For on-the-fly scanning, an optimal velocity was determined that minimizes vibration. This provides XANES scans in  $\sim$ 1 min at the P *K*-edge (2150 eV), down to  $\sim$ 10 s at the Ca *K*-edge (4040 eV). At slower scanning speeds, the stepper motor drive becomes less smooth and introduces vibration; at faster speeds, positional feedback may not fully keep up, although measurements are still possible at speeds of up to 75 eV s<sup>-1</sup> and 0.001 s per data point, provided the sample gives enough signal. Replicate scans are used to accumulate sufficient statistics. On-the-fly scanning is conducted via hardware synchronization between the motion control and detector systems to ensure that measurements of incident-beam intensity, fluorescence intensity and transmitted-beam intensity are integrated over precisely the same intervals, essential for EXAFS.

(4) Mirror 3. A sagittal cylinder with tunable bend for toroidal figure (Table 3) focuses up to 2.5 mrad of horizontal radiation to a submillimetre spot at the SSA. The new optic in this reconditioned system was manufactured with a radius of curvature to match the TES design. The toroid focuses to a set of JJ X-ray precision in-vacuum slits, which serve as the SSA.

(5) BPMs, necessary for continuous feedback control of beam position at the SSA, are active during use of the beam and must not significantly absorb the beam in this energy range. Horizontal and vertical feedbacks are treated separately. The vertical beam position is sensitive to thermal effects on the monochromator first crystal, and to motion of the monochromator when changing or scanning energy. Because there may be large vertical excursions when rapidly moving energy large distances, the vertical BPM must be transparent so as to always pass the beam to the horizontal BPM; the horizontal BPM must have a large vertical range. Vertical BPM sensors,  $\sim$ 2.5 m upstream of primary focus, consist of 0.8  $\mu$ m-thick aluminium foils (interchangeable with fine copper mesh screens) with photoelectron multipliers to measure proportional signal from the top and bottom halves of the beam (MacDowell *et al.*, 1989). This BPM is sensitive to  $\sim$ 5  $\mu$ m of vertical beam motion (200 nrad from the mono-

chromator). The photon shutter is downstream of the vertical BPM to continuously maintain heatload on the monochromator and to hold the vertical beam position.

The horizontal beam position is sensitive to source position and to residual mechanical roll of the monochromator as a function of energy. The horizontal BPM, located  $\sim 0.8$  m upstream of primary focus, consists of two edge-sensitive Si photodiodes bracketing the beam and measuring just its edges. The diodes have a vertical range of 23 mm but do not interfere with the usable portion of the beam. This BPM is sensitive to motion of  $\sim 2$   $\mu\text{m}$  (80 nrad from the monochromator).

(6) Microfocusing mirrors. A custom KB mirror system was designed in collaboration with P. Eng (U. Chicago) and P. Murray (IDT). This utilizes dynamically bent trapezoidal flat mirrors but is unusual in having the HFM upstream and in operating at a pitch of up to 16 mrad. Having the HFM upstream provides less demagnification horizontally than vertically but offers a larger dynamic range for user selection of horizontal spot size. In the lower-energy range, mirrors typically generate more scatter; it is therefore important that the HFM reflects the beam away from the fluorescence detector to reduce background. The HFM is also longer (320 mm *versus* 180 mm for the VFM) in order to accept a wider fan of radiation as horizontal divergence is greater than vertical. Acceptance is up to 4.5 mm  $\times$  1.7 mm (H  $\times$  V).

### 3. Endstation

The endstation consists of a small shielded hutch box, designed in collaboration with and constructed by Mark's Industrial Services. This chamber (Fig. 2) is fabricated as a welded aluminium shell lined on the inside with 1.06 mm lead covered with 0.03 mm copper to provide a clean background for the energy range between Cu *L* and *K* fluorescences. The hutch box holds a helium atmosphere isolated from beamline vacuum by a 12  $\mu\text{m}$ -thick polymer-coated beryllium window (Moxtek). For *in situ* measurements, feedthroughs deliver

electrical connections, power, thermocouple and gas/fluid to the sample position.

The sample is positioned by three stacked linear stages with 0.3  $\mu\text{m}$  minimum increment and *xy* travel of 100 mm  $\times$  100 mm. The sample plane is oriented at 45° to the incident beam, with the detector at 90°, in the classic XRF microprobe geometry. Scanning is always performed unidirectionally and against gravity, so as to provide the greatest mechanical stability and repeatability. On-the-fly scanning is conducted via hardware synchronization between the motion control and detector systems, and can be run at speeds of up to 11 mm s<sup>-1</sup> and pixel times as small as 0.001 s in region of interest (ROI) mode, provided the sample has sufficient signal. A visible-light microscope is positioned normal to the sample plane, with its focus coincident with the beam focus. A double right-angle prism is required to divert the optical path because of the close proximity of the VFM assembly.

The chamber is equipped with a Canberra ultralow-energy Ge fluorescence detector at 90° and in the plane of the beam. This detector has a high sensitivity for low count rates, a large 100 mm<sup>2</sup> detector area, very low background and excellent energy resolution (129 eV FWHM at 5900 eV). This enables sufficient discrimination of *e.g.* Al, Si and P fluorescences (at 1486, 1740 and 2010 eV). It is equipped with a CryoPulse cooling system, eliminating liquid nitrogen fills. Mounted just below that is a Vortex Si-drift detector angled upward at  $\sim 20^\circ$  toward the sample. This detector can handle higher count rates and has similar energy resolution. In general, because of lower fluorescence yields and smaller sampling depths, excessive count rates are much less of a problem than at higher energies. Either detector can be positioned close to the sample or retracted as needed. Both are customized with Moxtek beryllium windows for operation in helium without degradation of vacuum. Downstream of the sample is an ion chamber for transmission measurements (imaging, XAS), although not many samples are transparent to tender X-rays.

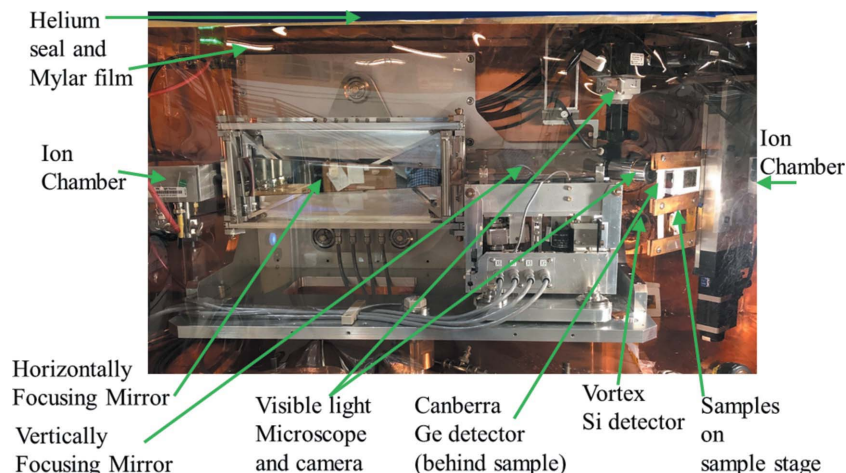


**Figure 2**  
Sample chamber and components.

### 4. Construction and commissioning

TES microfocusing endstation construction began at NSLS X15B. Although not an ideal proxy for TES, it was sufficient for initial testing. Installation (with help from M. Northrup and R. Tappero) included the chamber, KB mirrors, sample stage, detectors, controls, and required shielding and safety interlocks. Prototype motion controls, detection and on-the-fly scanning systems were developed using NSLS-II standard hardware and EPICS structure with help from Z. Yin, J. Ma, K. Feng and D. Poshka; prototype data-acquisition software was developed with help from U. Chicago CARS and R. Tappero; these pre-dated such developments at NSLS-II project beamlines. Successful commissioning provided a substantial head start for TES, its user community and science programs. After

shutdown of NSLS, the endstation and controls, as well as other beamline components, were moved from NSLS (Ivashkevych *et al.*, 2018) with assistance from G. Nintzel, M. Northrup, R. Tappero, R. Greene and M. Caruso.

On-the-floor construction at NSLS-II began in late 2015. Modification and staging of repurposed optical components were completed with help from G. Nintzel and M. Northrup; installation also benefited from the efforts of R. Tappero, J. Biancarosa, M. Maklary, E. Haas and J. Adams. C. De Silva led the setup of the beamline motion controls. First light was achieved on 18 August 2016. Commissioning was conducted in an overlapping phased approach; initial capabilities and energy range were commissioned first, additional capabilities continue to be commissioned in parallel with user operations so as to balance the need for scientific productivity and community engagement with eventual development of all planned capabilities.

Uncertainty and control of source position and beam trajectory became a significant issue early in the commissioning of TES, the first NSLS-II beamline to utilize a BM as its X-ray source. One of the inherent characteristics of NSLS-II is that it was designed to optimize beam brightness and source stability for insertion-device beamlines. As a result, the electron-beam orbit in the dipole region was initially unconstrained and does not have local BPMs. Because of the stability requirements for TES and the fact that the TES beamline itself is a powerful diagnostic of source position and stability, the accelerator team (led by G. Wang) undertook an extensive effort to work with the author to characterize the source and to successfully stabilize its position. This proved challenging because there are quadrupole and corrector magnets between the beamline's source point and the nearest electron BPMs (X-ray BPMs on the beamline are not useful with broad fans except at the focal point), and use of the beamline focus as a diagnostic of source position depends on beamline optics being correctly aligned to the source.

The initial modeled photon-beam trajectory, to which beamline components were surveyed and installed, was based on modeled magnetic field. Later calculations (by O. Chubar), based on actual measured BM field, revealed a horizontal discrepancy of 0.1 to 0.2 mrad. This was further complicated by the fact that at this point in the BM field the photon beam is produced as the tangent to a curve of changing radius. Thus uncertainty in electron-beam orbit results in uncertainty in source point along the arc as well as both lateral position and angle.

The key task was therefore identification of an acceptable reference orbit and establishment of means to maintain it. Iterative alignment of beamline optics to different electron-beam orbit positions eventually converged on a preferred orbit. Modeling algorithms developed by G. Wang and Y. Hidaka incorporate values from electron BPMs and magnet power settings to interpolate a source-point position and photon-beam angle. Periodic (tens of minutes) adjustment of local orbit is then used to maintain these values within tolerance and to return to the correct position after a beam fill. In conjunction with these efforts and other observations around

the ring, an approximately diurnal fluctuation of orbit diameter was found to be the result of lunar tidal influences. This fluctuation was addressed by implementation of a global radiofrequency feedback. Once these measures were fully tested and implemented in late 2017, the source delivered the stability required for TES. Source horizontal position is the most critical parameter and in practice is now routinely maintained within  $\pm 5 \mu\text{m}$  over  $>24 \text{ h}$  and across most beam dump/fill cycles. This was a lengthy learning experience for all, and a noteworthy example of teamwork between beamline and accelerator staff.

Once the source position and beam trajectory were locked in, then full alignment of the beamline could proceed. This included alignment of the monochromator and Mirror 3, establishment of zero for monochromator roll for its entire angular range, and repositioning of beamline components to the correct beam centerline. This subsequently presented the opportunity to characterize monochromator residual mechanical deviations with energy. Although small, with a 28 m lever arm even a few  $\mu\text{rad}$  requires compensation. Implementation of the ultrafine roll-adjustment modification to the monochromator addressed this residual horizontal motion, and continuous feedback maintains horizontal beam trajectory to within 100 nrad.

Initial commissioning used Si(111) monochromator crystals for the 2.0 to 5.5 keV energy range. InSb(111) will be used primarily for the Si *K*-edge at 1.8 keV. One set of InSb crystals, which had been successfully tested at X15B, were found to be inadequate for the very small NSLS-II source and long beamline distances at TES. Because of poor surface flatness and high mosaicity, it was impossible to achieve acceptable focus. A new set is ready for testing in 2019.

Because of intense pressure from the user community, commissioning activities were balanced with early service to users. First users were served in November 2016. Official User Readiness was achieved on 23 October 2017, and full energy scanning capabilities were made available in May 2018. In its first year of operation since User Readiness, TES served 133 unique individuals as users at the beamline.

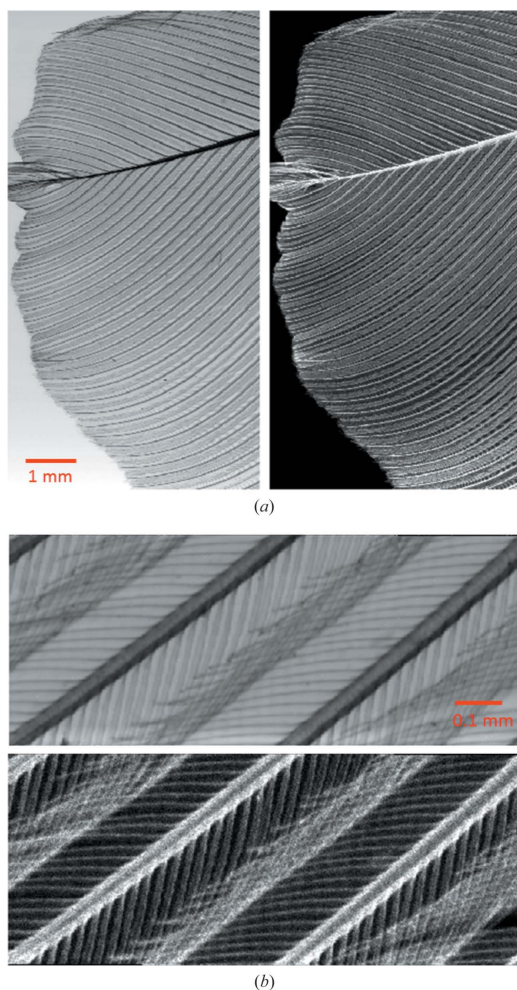
## 5. Example measurements

Early results demonstrate beamline capabilities and suitability for various applications. During commissioning of the TES endstation and prototype controls at NSLS X15B, Yu *et al.* (2015) determined the microscale redistribution and speciation of S *in situ* in a Li-S battery cell during the first charge cycle; Leri *et al.* (2015) used imaging and  $\mu\text{-XANES}$  to identify two natural organochlorine species in marine particulates, which proved essential for interpretation of previously measured bulk spectra; and Moon *et al.* (2016) measured the distribution and local speciation of S in a sulfur-polymer green concrete. Gamble (2017) included data from both X15B and TES. Initial results at NSLS-II followed: for example, Vidavsky *et al.* (2018) identified hydroxyapatite biomineral in microcalcifications associated with breast cancer. Standard characterization methods confirmed the technical perfor-

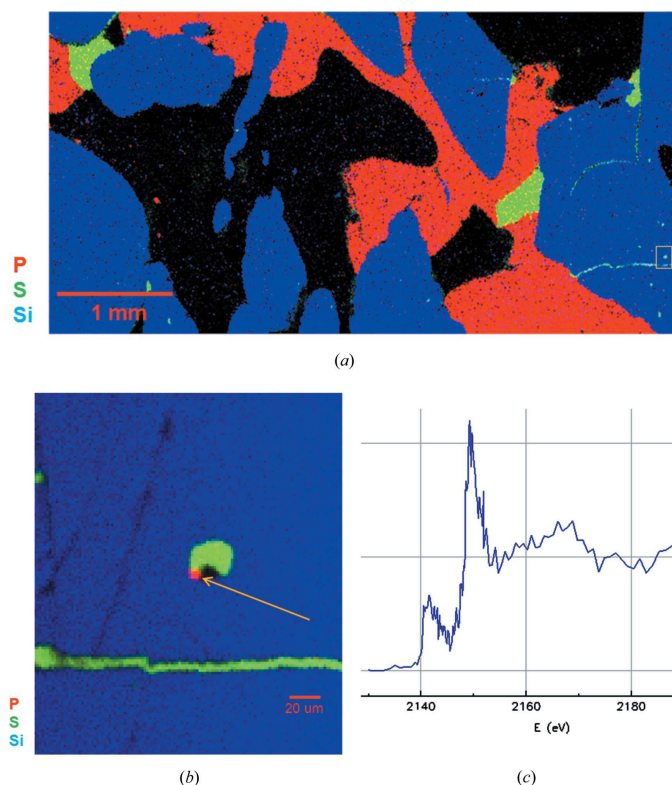
mance of TES. The following representative measurements illustrate its imaging, spatially resolved and *in situ* XAS capabilities with respect to user needs.

A bird's feather is a hierarchical construction with features from the centimetre to nanometre scale and contains S in its composition, so it is an ideal natural test material for TES to demonstrate large- to small-scale imaging and spot size (Fig. 3). Another example, characterizing multi-scale heterogeneity and element-specific chemistry in a meteorite section, is shown in Fig. 4.

In geologic materials, it is often important to characterize both light and heavy elements at the same time. However, using higher-energy incident beam for both low-energy and high-energy fluorescence at the same time is problematic. The effective sampling depth is much less for lighter elements, so the volumes sampled will differ greatly. Detection of both low-energy and high-energy fluorescence at the same time is challenging. Absorption cross-sections decrease at higher incident energies. Detection of lower-energy trace elements



**Figure 3** Feather of a gray catbird. (a) Large-area coarse-resolution image in (left) transmission contrast and (right) S  $K\alpha$  fluorescence. Incident energy 2700 eV, beam spot size  $10\ \mu\text{m} \times 5\ \mu\text{m}$  and pixel size  $10\ \mu\text{m}$ . (b) Higher-resolution image, spot size  $3\ \mu\text{m} \times 3\ \mu\text{m}$  and pixel size  $2\ \mu\text{m}$ ; (top) S fluorescence and (bottom) transmission contrast. Note that parts of the sample are not all in the same plane.

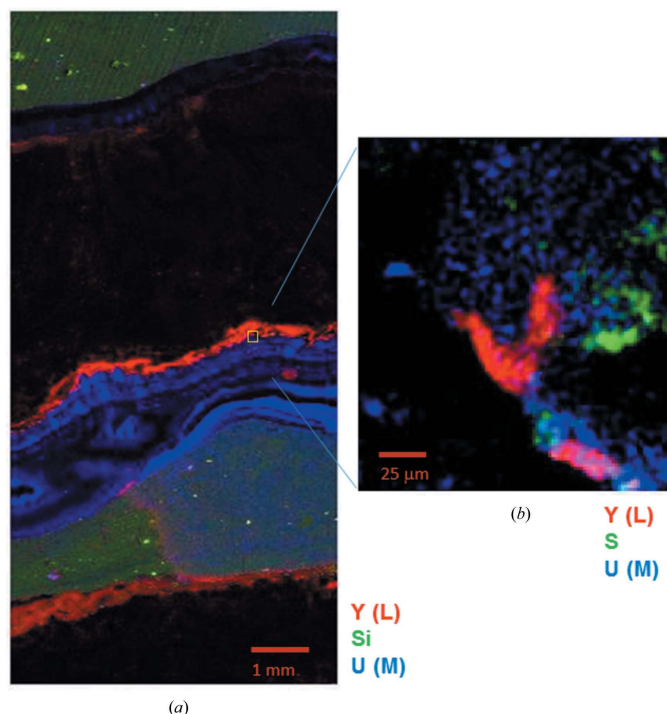


**Figure 4** Meteorite polished section. (a) Fast survey fluorescence image of a  $5.1\ \text{mm} \times 2.6\ \text{mm}$  area, measured using a  $10\ \mu\text{m} \times 5\ \mu\text{m}$  beam,  $9\ \mu\text{m}$  pixels and  $0.002\ \text{s}$  per pixel ( $4.7\ \text{mm}\ \text{s}^{-1}$  scan speed). Flux to the sample is  $\sim 7 \times 10^9\ \text{photons}\ \text{s}^{-1}$  with an incident energy of 2700 eV. Red (P fluorescence) indicates Fe,Ni phosphide, green (S fluorescence) is Fe sulfide, blue (Si fluorescence) is olivine mineral grains and black is Fe,Ni metal. (b) Fine features in marked area using  $\sim 2\ \mu\text{m}$  beam and  $1.56\ \mu\text{m}$  pixels. At this scale, this sample's poor surface polish is evident at boundaries. (c) Phosphorus  $K$ -edge XANES of spot in (b) with  $\sim 2\ \mu\text{m}$  beam, a sum of eight scans of 45 s each; flux is  $\sim 9 \times 10^8\ \text{photons}\ \text{s}^{-1}$ .

will be hampered by the dominant fluorescence of major elements such as Fe or Ca. In contrast, setting the incident-beam energy below the  $K$ -edge of Ca is particularly helpful for carbonates, while the use of lower-energy  $L$  and  $M$  fluorescence makes it possible to simultaneously measure many heavier elements (Fig. 5).

A further advantage of using lower-energy fluorescence lines is that spatial resolution is not degraded by sample thickness. A higher-energy beam effectively samples material to a depth of tens to hundreds of micrometres. So, for a given pixel, the fluorescence measured is of a volume including both surface and buried features; at the typical  $45^\circ$  geometry this means an image is also blurred horizontally. In order to fully achieve the spatial resolution defined by the beam spot size, sample thickness must be comparable to spot size. However in the tender-energy range, for most sample materials the effective sampling depth is less than a few micrometres. Thus, lateral resolution is not compromised by sample thickness. This makes sample preparation easier and simplifies quantitative XRF analysis by eliminating thickness as an uncertain variable.

Beam stability across the full routine energy range is essential for users to go to any absorption edge without

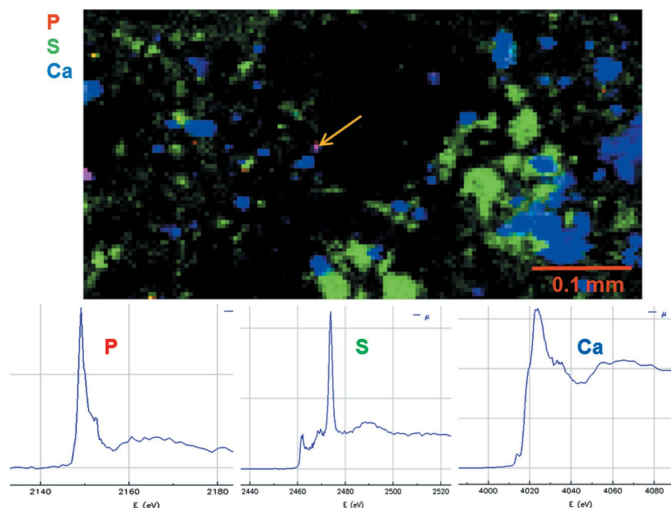

**Figure 5**

Characterization of Si, S, Y and U in a rock section. An incident-beam energy of 3555 eV optimizes  $U M\alpha$  fluorescence (at the  $M_5$  edge), stimulates  $Y L\alpha$  fluorescence (the  $L_3$  edge is 2080 eV), as well as  $K$  fluorescences from S, Si and Al ( $K$ -edges 2480, 1840 and 1560 eV), but remains below the major-element Ca  $K$ -edge (4040 eV). (a) XRF image of Y [ $L(\alpha,\beta)$ ] fluorescence at 1994 and 1998 eV in red, Si ( $K\alpha$  at 1740 eV) in green and U ( $M\alpha$  at 3164 eV) in blue. The beam size is  $10 \mu\text{m} \times 5 \mu\text{m}$ , the pixel size is  $25 \mu\text{m}$  and the flux is  $\sim 10^{10}$  photons  $\text{s}^{-1}$ . Different minerals present include calcite  $\text{CaCO}_3$ , appearing mostly black; fluorite  $\text{CaF}_2$  with locally variable trace U content, appearing patterned blue; Al-Si clay minerals, appearing greenish or blue-green if U is present; and a carbonate of Y, appearing red. (b) A high-resolution XRF image of Y in red, S ( $K\alpha$  at 2310 eV) in green and U in blue, of the small area indicated. The beam size is  $\sim 2 \mu\text{m}$ , the pixel size is  $1.5 \mu\text{m}$  and the flux is  $\sim 10^9$  photons  $\text{s}^{-1}$ . Sample provided by E. Rasbury (Piccione *et al.*, 2019).

needing to adjust or realign the optics, with assurance that the beam is still on the same spot independent of energy. A good test of this is a single energy scan spanning several absorption edges; such scans are possible at TES, covering a range as large as from 2.0 to 5.5 keV, even on compositionally and topographically heterogeneous samples, using any available beam size. A more traditional example of XANES at multiple edges for a single-pixel particle is shown in Fig. 6.

One of the primary achievements of TES is the ability to measure full EXAFS, at microbeam resolution in a heterogeneous sample, even at the very challenging P  $K$ -edge (Fig. 7). For Si(111) monochromator crystals, scanning from 2130 to 2800 eV covers an angle range from  $\sim 70$  to  $44^\circ$ , with a 36 mm translation of the second crystal.

An important but experimentally challenging part of the TES mission is *in situ/operando* catalysis and electrochemistry. An example measurement (Fig. 8) utilized a reaction cell designed with a thin window, a minimized beam path through solvent, and insulation to reduce heat transfer to the helium environment. In addition, measuring P fluorescence in a sili-


**Figure 6**

XRF image of P (red), S (green) and Ca (blue) in a meteorite thin section shows a small grain (single  $4 \mu\text{m}$  pixel) with high P and Ca. XANES spectra of this location were measured at P, S and Ca edges with a  $2 \mu\text{m} \times 3 \mu\text{m}$  beam. The sample was provided by the Field Museum of Natural History, Chicago, IL, USA, courtesy of P. Heck, S. Simon, S. Wirick and S. Sutton.

cate matrix faced the combined challenge of high Si fluorescence signal and the preferential absorption of P fluorescence by Si. Other microreactors are under development. Various battery cells, including button and capillary types, have also been successfully tested at TES *in situ* under charge cycling.

## 6. Conclusions

The TES beamline for tender-energy spatially resolved X-ray absorption spectroscopy and X-ray fluorescence imaging at the National Synchrotron Light Source II (NSLS-II) at Brookhaven National Laboratory is now operational and available for general user proposals. This new beamline offers a user-tunable spot size of  $\sim 2$ – $25 \mu\text{m}$ , a routine energy range of 2.0–5.5 keV, and the capabilities of XRF imaging and spatially resolved XAS, all in a non-vacuum (helium) environment. The unique optical design of TES enables microbeam XAS in heterogeneous materials with no significant beam motion at the sample position. As a result, XAS, including full EXAFS and XAS of multiple absorption edges, can be obtained from microscale particles or regions that are the same size as the probe beam. *In situ* or *operando* measurements are possible in small reaction cells or microreactors. Capabilities yet to be commissioned include the energy range below 2 keV for XAS at the  $K$ -edges of Si, Al and Mg using alternate monochromator crystals.

## Acknowledgements

The complete development of a beamline requires effort from very many people; specific individual contributions are noted throughout this text. The author is especially grateful for the assistance and discussions of R. Tappero, and wishes to

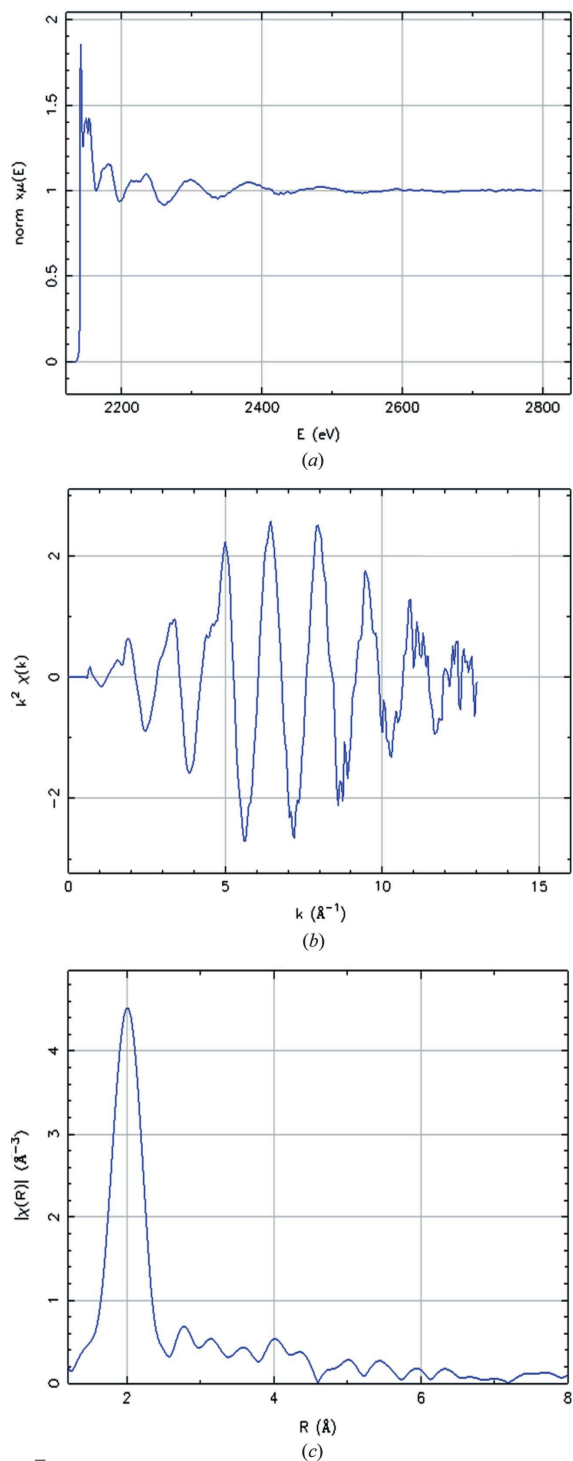


**Figure 7**

Microbeam EXAFS, P *K*-edge, of a Fe,Ni phosphide grain in a heterogeneous meteorite section. The beam size is  $10\ \mu\text{m} \times 5\ \mu\text{m}$ . (a) Normalized energy spectrum; (b)  $k^2$ -weighted EXAFS; and (c) Fourier transform, showing pronounced first shell (9 Fe/Ni) and complex higher shells to  $\sim 4\ \text{\AA}$ . It is noteworthy that this sample contains some S, but the detector resolution is sufficient to separate P from S.

acknowledge the contributions of safety personnel (including L. Stiegler and B. Chmiel), utilities teams (A. Boerner, G. Ganetis and J. Gosman), controls and computational teams, riggers, technicians, various design and project reviewers

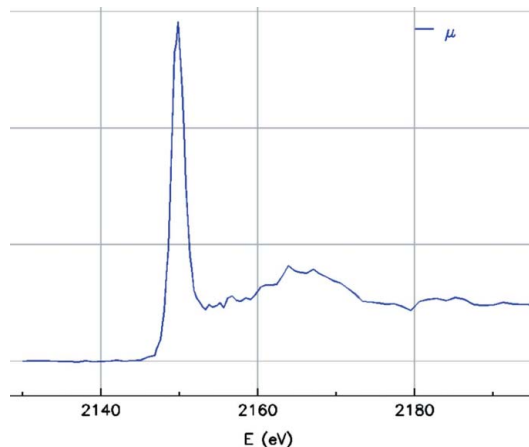


**Figure 8**

P XANES of a phosphate/silicate catalyst measured in a prototype small reaction cell, under *operando* conditions at  $40^\circ\text{C}$ , 1 atm, with reactants and products in organic solvent; a  $5\ \mu\text{m} \times 10\ \mu\text{m}$  beam, a sum of 10 scans and 40 s each were used. Data courtesy of W. Zheng, Catalysis Center for Energy Innovation, and U. Delaware.

(in particular A. Macdowell), project advisors (especially D. Hesterberg and J. Rodriguez) and the user community.

### Funding information

TES was funded by a combination of the BDN Project (NSLS-II operations, US Department of Energy contract DE-SC0012704) and resources provided by partner users: the Tender Energy Microspectroscopy Consortium of P. Northrup (Lead Scientist), J. Brandes, G. Flynn, D. Hesterberg, P. Lam, S. Myneni, J. Rakovan, E. Rasbury, R. Reeder, M. Schoonen, D. Sparks, G. Waychunas and D. Weidner, supported by member institutions. Instrumentation was directly funded in part by NSF (EAR-1128957), DOE (DE-FG02-12ER16342) and NASA (NNX13AD12G), as well as Lucent Technologies. NSLS operations were under contract DE-AC02-98CH10886.

### References

- Akabayov, B., Doonan, C. J., Pickering, I. J., George, G. N. & Sagi, I. (2005). *J. Synchrotron Rad.* **12**, 392–401.
- Baturina, O., Gould, B., Northrup, P. & Swider-Lyons, K. (2013). *Catal. Today*, **205**, 106–110.
- Bolin, T., Birdwell, J., Lewan, M., Hill, R., Grayson, M., Mitra-Kirtley, S., Bake, K., Craddock, P., Abdallah, W. & Pomerantz, A. (2016). *Energy Fuels*, **30**, 6264–6270.
- Diaz, J., Ingall, E., Benitez-Nelson, C., Paterson, D., de Jonge, M., McNulty, I. & Brandes, J. (2008). *Science*, **320**, 652–655.
- Gamble, A. (2017). *Speciation and Reactivity of Phosphorus and Arsenic in Mid-Atlantic Soils*. PhD thesis, University of Delaware, Newark, USA.
- George, G. & Gorbaty, M. (1989). *J. Am. Chem. Soc.* **111**, 3182–3186.
- Hussain, M. (2014). *8th International Conference on Mechanical Engineering Design of Synchrotron Radiation Equipment and Instrumentation (MEDSI2014)*, 20–24 October 2014, Melbourne, Victoria, Australia ([https://medsi.lbl.gov/2014\\_ALS-156.html](https://medsi.lbl.gov/2014_ALS-156.html)).
- Ivashkevych, O., Nintzel, G., Ma, J., Carr, G., Guerrero, C., De Silva, L., Ehrlich, S., Tappero, R., Poshka, D., Fukuto, M., Abeykoon, M., Greene, R., Adams, J., Northrup, P. & Yin, Z. (2018). *Proceedings of the 16th International Conference on Accelerator and Large*

- Experimental Physics Control Systems (ICALPECS 2017)*, Barcelona, Spain, 8–13 October 2017. TUPHA003.
- Lanzirrotti, A., Fitts, J., Jacobsen, C., Northrup, P., Parise, J., Ravel, B., Reeder, R. & Sutton, S. (2007). *An Initial Assessment of the Needs of the NSLS-II Molecular Environmental Sciences/Low-Temperature Geochemistry User Community*, <http://citeseerx.ist.psu.edu/viewdoc/download?doi=10.1.1.459.6931&rep=rep1&type=pdf>.
- Leri, A., Mayer, L., Thornton, K., Northrup, P., Dunigan, M., Ness, K. & Gellis, A. (2015). *Nat. Geosci.* **8**, 620–624.
- Li, Y., Zakharov, D., Zhao, S., Tappero, R., Jung, U., Elsen, A., Baumann, P., Nuzzo, R., Stach, E. & Frenkel, A. (2015). *Nat. Commun.* **6**, 7583.
- Liu, C., Bolin, T., Northrup, P., Lee, S., McEnally, C., Kelleher, P., Pfefferle, L. & Haller, G. (2014). *Top. Catal.* **57**, 693–705.
- MacDowell, A. A., Celestre, R. S., Howells, M., McKinney, W., Krupnick, J., Cambie, D., Domning, E. E., Duarte, R. M., Kelez, N., Plate, D. W., Cork, C. W., Earnest, T. N., Dickert, J., Meigs, G., Ralston, C., Holton, J. M., Alber, T., Berger, J. M., Agard, D. A. & Padmore, H. A. (2004). *J. Synchrotron Rad.* **11**, 447–455.
- MacDowell, A., Hashizume, T. & Citrin, P. (1989). *Rev. Sci. Instrum.* **60**, 1901–1904.
- MacDowell, A., West, J., Greaves, G. & Van der Laan, G. (1988). *Rev. Sci. Instrum.* **59**, 843–852.
- Martin, R., Shotyk, W., Naftel, R., Ablett, J. & Northrup, P. (2010). *X-ray Spectrom.* **39**, 257–259.
- Moon, J., Kalb, P., Milian, L. & Northrup, P. (2016). *Cem. Concr. Compos.* **67**, 20–29.
- Northrup, P. (2013). *Proceedings GeoSciences PI Meeting: Geochemical Probes and Processes*, p. 10. [https://science.energy.gov/~/media/bes/csgb/pdf/docs/Chemical%20Transformations/Geosciences/2013\\_Geochemical\\_Probes\\_and\\_Processes\\_Program.pdf](https://science.energy.gov/~/media/bes/csgb/pdf/docs/Chemical%20Transformations/Geosciences/2013_Geochemical_Probes_and_Processes_Program.pdf)
- Northrup, P., Bare, S., Brandes, J., Buonassisi, T., Chen, J., Croft, M., DiMasi, E., Frenkel, A., Hesterberg, D., Hulbert, S., Khalid, S., Myneni, S., Rasbury, E., Ravel, B., Reeder, R., Rodriguez, J., Sparks, D., Stojanoff, V. & Waychunas, G. (2010). *Tender Energy X-ray Spectroscopy (TES): A facility for high performance and in situ X-ray absorption spectroscopy and spatially resolved XAS of structured materials, optimized for the "tender" energy range from 1.2 up to 8 keV*. NSLS-II Beamline Development Proposal, New York, USA.
- Northrup, P., Brandes, J., Hesterberg, D., Lam, P., Rakovan, J., Rasbury, E., Reeder, R., Schoonen, M. & Sparks, D. (2013). *Development of a Tender-Energy Microspectroscopy and Imaging User Facility for Earth Sciences at NSLS and NSLS-II*, Grant EAR-1128957, NSF Earth Sciences Instrumentation and Facilities Program, [https://nslgov/awardsearch/showAward?AWD\\_ID=1128957&HistoricalAwards=false](https://nslgov/awardsearch/showAward?AWD_ID=1128957&HistoricalAwards=false).
- Northrup, P. & Flynn, G. (2012). *A New Tender-Energy X-ray Microprobe User Facility for Analysis of Returned Samples*, Grant NNX13AD12G, NASA Laboratory Analysis of Returned Samples Program, <https://nspires.nasaprs.com/external/viewrepositorydocument/cmdocumentid=352913/solicitationId=%7BFB48203E-A59C-0E9A-5CA3-3F9C3430A54C%7D/viewSolicitationDocument=1/LARS12%20Selections.pdf>.
- Northrup, P., Lanzirrotti, A. & Celestian, A. (2007). *Synchrotron Radiat. News*, **20**(3), 6–13.
- Northrup, P., Leri, A. & Tappero, R. (2016). *Protein Pept. Lett.* **23**, 300–308.
- Piccione, G., Rasbury, E., Elliott, B., Kyle, J., Jaret, S., Acerbo, A., Lanzirrotti, A., Northrup, P., Wooton, K. & Parrish, R. (2019). *Geosphere*. Accepted.
- Punshon, T., Tappero, R., Ricachenevsky, F., Hirschi, K. & Nakata, P. (2013). *Plant J.* **76**, 627–633.
- Riquelme, F., Northrup, P., Ruvalcaba-Sil, J., Stojanoff, V., Siddons, P. D. & Alvarado-Ortega, J. (2014). *Appl. Phys. A*, **116**, 97–109.
- Rowen, M., Waldhauer, A. & Pianetta, P. (1986). *Nucl. Instrum. Methods Phys. Res. A*, **246**, 440–443.
- Sanchez del Rio, M., Canestrari, N., Jiang, F. & Cerrina, F. (2011). *J. Synchrotron Rad.* **18**, 708–716.
- Vidavsky, N., Kunitake, J., Chiou, A., Northrup, P., Porri, T., Ling, L., Fischbach, C. & Estroff, L. (2018). *Biomaterials*, **179**, 71–82.
- Voyles, P., Chadi, D. J., Citrin, P. H., Muller, D., Grazul, J., Northrup, P. & Gossman, H.-J. (2003). *Phys. Rev. Lett.* **91**, 125505.
- Yu, X., Pan, H., Zhou, Y., Northrup, P., Xiao, J., Bak, S., Liu, M., Nam, K., Qu, D., Liu, J., Wu, T. & Yang, X. (2015). *Adv. Energy Mater.* **5**, 1500072.